Journal of Materials Chemistry C

Accepted Manuscript

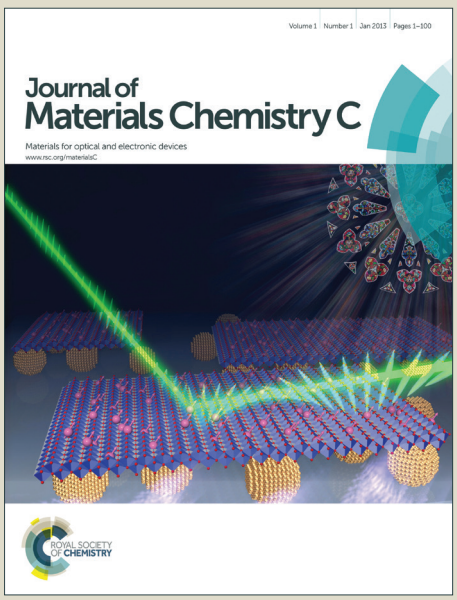

ROYAL SOCIETY OF CHEMISTRY

www.rsc.org/materialsC

Journal Name

RSCPublishing

ARTICLE

Hot injection thermolysis of heterometallic pivalate clusters for the synthesis of monodisperse zinc and nickel ferrite nanoparticles.

Cite this: DOI: 10.1039/x0xx00000x

Khadijat. O. Abdulwahab,[a] Mohammad A. Malik,[a] Paul O'Brien,[a,b] Grigore A. Timco,[a] Floriana Tuna,[a,c] Richard E. P. Winpenny,[a,c] Richard A.D. Pattrick,[d] Victoria S Coker,[d] Elke Arenholz[e]*

Received 00th January 2012,
Accepted 00th January 2012

DOI: 10.1039/x0xx00000x

www.rsc.org/

Abstract

The heterometallic pivalate clusters- $[Zn_4Fe_2O_2(O_2C^tBu)_{10}]$ **(1)** and $[Fe_2NiO(O_2C^tBu)_6(HO_2C^tBu)_3]$ **(2)** have been used as single source precursors to synthesise monodispersed zinc ferrite ($ZnFe_2O_4$) and nickel ferrite ($NiFe_2O_4$) nanoparticles respectively. The precursors were thermolysed with a mixture of oleylamine and oleic acid in either diphenyl ether or benzyl ether as the solvent at their respective boiling points of 260 and 300 °C. The effect of reaction time, temperature and concentration (0.25 or 0.50 mmol) on the stoichiometry, the phase or morphology of the nanoparticles were studied. TEM showed that highly monodispersed spherical nanoparticles of zinc ferrite (3.2 ± 0.2 nm) and nickel ferrite (3.3 ± 0.2 nm) respectively were obtained from **(1)** and **(2)** using 0.50 mmol precursor concentration at 260 ºC. The decomposition of the precursors at 0.25 mmol and 300 °C gave larger nanoparticles of zinc ferrite (5.6 ± 0.5 nm) and nickel ferrite (5 ± 0.6 nm) from **(1)** and **(2)** respectively. The effect of reaction time was investigated for both precursors at 0.25 mmol by withdrawing aliquots at 5 minutes, 15 minutes, 30 minutes, 1 hour and 2 hours. Aliquots withdrawn at reaction times of less than 1 hour contain traces of iron oxide whilst only pure cubic zinc or nickel ferrite was obtained after one hour. Magnetic measurements revealed that all the ferrite particles are superparamagnetic at room temperature with high saturation magnetisation values. XMCD confirmed that in nickel ferrite particles, most of the Ni^{2+} cations are in the octahedral site. The hysteresis loop observed on the zinc ferrite nanoparticles indicated that there is cation redistribution, this is further evident in the XMCD analysis and EPMA result.

Introduction

Monodisperse magnetic nanoparticles possessing unique properties have become significant in science and technology in recent times which is especially true for those of ferrite spinels. Their study has established relationships between their magnetic properties and their chemical structure. These properties depend on the nature of the ions, their valency and their cation distribution between octahedral and tetrahedral sites.[1,2] Nickel ferrite nanoparticles are an important material with the inverse spinel structures typical with ferromagnetic properties, high electrical resistivity, moderate saturation magnetisation, and their ready availability.[3,4] These properties make the material suitable for applications in various fields such as in recording tapes, drug delivery, Magnetic Resonance Imaging (MRI), gas sensors, environmental remediation, bio separation, gas sensors, catalysis, transformers and AC generators.[1,4–11] A number of synthetic routes have been developed for nickel ferrite nanoparticles including: co-precipitation[12,13] hydrothermal,[14–21] pulsed wire discharge,[1] sol-gel method,[22,23] flow reactor[24] microbial reduction[25] and thermal decomposition.[26–29] Research has shown that the properties of such particles are influenced by their monodispersity which

inturn depends on the method of preparation.

Zinc ferrite nanoparticles show significant differences in magnetic properties as compared to the bulk material. Bulk zinc ferrite has a normal spinel structure with the nonmagnetic Zn^{2+} ions in the tetrahedral sites and Fe^{3+} ions in the octahedral sites leading to an antiferromagnetic interactions at about 10 K. In the zinc ferrite nanoparticles, however, there could be rearrangement of cations due to the high surface area of nanoparticles. This migration of cations in turn creates ferrimagnetic exchange interactions leading to a higher saturation magnetisation[30–32] Such particles have found applications in (MRI),[33] gas sensors, absorbent material in gas desulphurization,[34] and photocatalysts.[35] These applications have prompted the development of different synthetic methods including co-precipitation,[36,37] sol-gel,[38] biological,[39,40] micro-emulsion[41] and thermal decomposition.[15,28,32,41]

Only few reports have been made on the use of single source precursors for the synthesis of monodispersed nickel or zinc

ferrite nanoparticles.[15,27,29] In this paper, we report the first use of heterometallic pivalate clusters for the direct synthesis of spherical monodispersed nickel and zinc ferrite nanoparticles by a hot injection thermal decomposition method. The effect of concentration, temperature and reaction time on the morphology, stoichiometry and the phase of the particles formed is described. The particles were characterized by Powder X-ray Diffraction (p-XRD), Transmission Electron Microscopy (TEM), High Resolution Transmission Electron Microscopy (HRTEM), Inductively Coupled Plasma (ICP) and the magnetic properties were investigated using a Superconducting Quantum Interference Device (SQUID). X-ray Magnetic Circular Dichroism (XMCD, combined with Electronprobe Microanalysis (EPMA) were also used to determine cation site occupancies in the ferrite nanoparticles.

Experimental

All preparations were performed under an inert atmosphere of dry nitrogen using standard Schlenk techniques. All reagents were purchased from Sigma-Aldrich and used as received. Solvents were distilled prior to use. Magnetic measurements were determined with a Quantum Design MPMS-XL SQUID magnetometer equipped with a 7 T magnet. Zero-field cooled (ZFC) and Field-cooled (FC) magnetization were recorded over 5-300 K temperature range with an applied field of 100 Oe. XMCD was achieved by mounting the ferrite nanoparticles on carbon tape attached to a copper sample probe and measured at the Fe and Ni $L_{2,3}$ X-ray absorption spectral (XAS) edges in vacuum using total electron yield (TEY); it has an effective probing depth of ~3-4 nm. XMCD spectra are then obtained as the difference between two XAS spectra recorded in two opposite applied magnetic fields of ± 0.6 T (parallel and antiparallel to the beam direction). These data were then compared to calculated spectra for the appropriate elemental sites and oxidation states, see Patrick *et al*.[43] and van der Laan & Kirkman[44] for details. EPMA was undertaken using a Cameca Camebax SX100, a beam size of 2 µm, a beam current of 20na, an accelerating voltage of 15KeV, wavelength, spectrometry and pure metal standards; samples were mounted on carbon tape.

Synthesis of Precursors

Iron-zinc pivalate **$[Zn_4Fe_2O_2(O_2C^tBu)_{10}]$ (1)** was synthesised following the procedure described in literature[45] and the synthesis of the iron-nickel pivalate **$[Fe_2NiO(O_2C^tBu)_6(HO_2C^tBu)_3]$ (2)** was adapted from our previous work**.**[46] A brief outlines of the syntheses is given below:

Compound 1

A three stage process was employed for the synthesis of this cluster.

Stage 1: $[Fe_3O(O_2C^tBu)_6(H_2O)_3]O_2C^tBu$ was obtained according literature procedure.[47]

Stage 2**:** $[Zn(O_2C^tBu)_2]_n$

$Zn(OAc)_2{\cdot}2H_2O$ (5.0 g, 22.8 mmol) and HO_2C^tBu (30.0 g, 294 mmol) were heated over 2 hours at 160 - 170 °C while stirring. The fine crystals formed were washed with toluene and hexane and dried in air.

Stage 2: $Zn_4Fe_2O_2(Piv)_{10}$

$[Zn(O_2C^tBu)_2]_n$ (3.0 g) and $[Fe_3O(O_2C^tBu)_6(H_2O)_3]$ O_2C^tBu (1.5 g, 1.6 mmol) were heated to reflux in toluene (50 ml) for 1 hour. The light-yellow solution was filtered and acetonitrile (50 ml) was added. A pale-yellow product crystallised on cooling to room temperature was filtered off, washed with a 1:1 mixture toluene/acetonitrile and dried in air.

$[Fe_2NiO(O_2C^tBu)_6(HO_2C^tBu)_3]$ (2)

Iron nitrate nonahydrate (10.0 g, 24.8 mmol) and pivalic acid (50.0 g, 490 mmol) were heated while stirring at 160 – 165 °C (~ 5 hours), until the elimination of NO_2 has finished. Then the flask was cooled to 100 °C and the basic nickel carbonate (1.5 g, 12.6 mmol) was added and the reaction was kept under a slow flow of nitrogen. This was followed by the addition of toluene (25 ml). After 1 hour, the temperature of oil bath was increased to 165 °C in order to remove the toluene and the reaction mixture was kept at this temperature for 7 hours. Next, the flask was cooled to 60 - 70 °C and acetonitrile (50 ml) was added in small portion while stirring. After 1 hour, the product was filtered, washed with acetonitrile (3-4 x 25 ml) and dried in air.

Synthesis of nanoparticles

The nanoparticles were synthesized by the hot injection thermal decomposition method. Reaction parameters including temperature, concentration and reaction time were varied for each precursor. The effect of concentration was studied at a fixed temperature of 260 °C at 0.25 mmol and 0.50 mmol. The temperature dependence was investigated at 0.25 mmol in either diphenyl ether or benzyl ether as the solvent at their respective boiling points of 260 and 300 ºC. The reaction time was studied at 260 °C using 0.25 mmol precursor by withdrawing aliquots at 5 minutes, 15 minutes, 30 minutes, 1 hour and 2 hours. In a typical experiment, a mixture of oleylamine (27 mmol), oleic acid (27 mmol) with either diphenyl ether or benzyl ether (20 ml) was degassed at 100 ºC under vacuum for 30 minutes and then heated to the boiling point of the solvent under nitrogen. The required concentration of the precursor (0.25 or 0.50 mmol) was dissolved in the appropriate solvent (10 ml) and injected into the solution of the hot mixture. The reaction was maintained at 230 ºC for 2 hours. The dark mixture was allowed to cool and methanol was added to precipitate the nanoparticles which were then isolated by centrifugation. The residue was washed with methanol thrice and then redispersed in toluene.

Characterisation of nanoparticles

Powder X-ray diffraction studies were performed on a Bruker Discover 8 diffractometer with a Co- Kα radiation. TEM samples were prepared by placing 1 or 2 drops of the nanoparticles dispersion on a lacey carbon copper grids. TEM and HRTEM were performed on Tecnai F30 FEG TEM instrument at an accelerating voltage of 300 Kv. For XMCD, the Fe and Ni $L_{2,3}$-edge XAS spectra were collected on beam line 4.0.2 of the Advanced Light Source (ALS), Lawrence Berkeley National Laboratory, California, USA.

Results and discussions

The ferrite nanoparticles obtained from the precursors were analysed by powder X-ray diffraction (p-XRD), TEM, ICP, EPMA, XMCD and SQUID. The effect of the different

parameters namely reaction time, temperature and concentration on the morphology and phase of the nanoparticles are described.

Reaction time

The effect of reaction time was studied for both precursors by injecting 0.25 mmol concentrations in oleylamine, oleic acid and diphenyl ether at 260 °C and subsequently, aliquots were withdrawn at 5 minutes, 15 minutes, 30 minutes, 1 hour and 2 hours.

The p-XRD pattern of nanoparticles obtained from $[Zn_4Fe_2O_2(O_2C^tBu)_{10}]$ showed that the intensity of the peaks increases with time (Fig. 1(a)). No product was formed at 5 minutes whilst the pattern obtained at 15 minutes was broad. Distinct peaks begin to appear distinct at 30 minutes and were predominantly of hexagonal iron oxide (ICDD Card No: 04-013-3305). The peaks obtained after 1 hour were of cubic zinc iron oxide (ICDD Card No: 04-006-1956). The diameter and crystallinity of the particles increases over time as observed in the images taken at 30 minutes (3.6 ± 0.4 nm), 1 hour (4.2 ± 0.8 nm) and at 2 hours (5.1 ± 0.7 nm) (Fig. 1(b)-(d)).

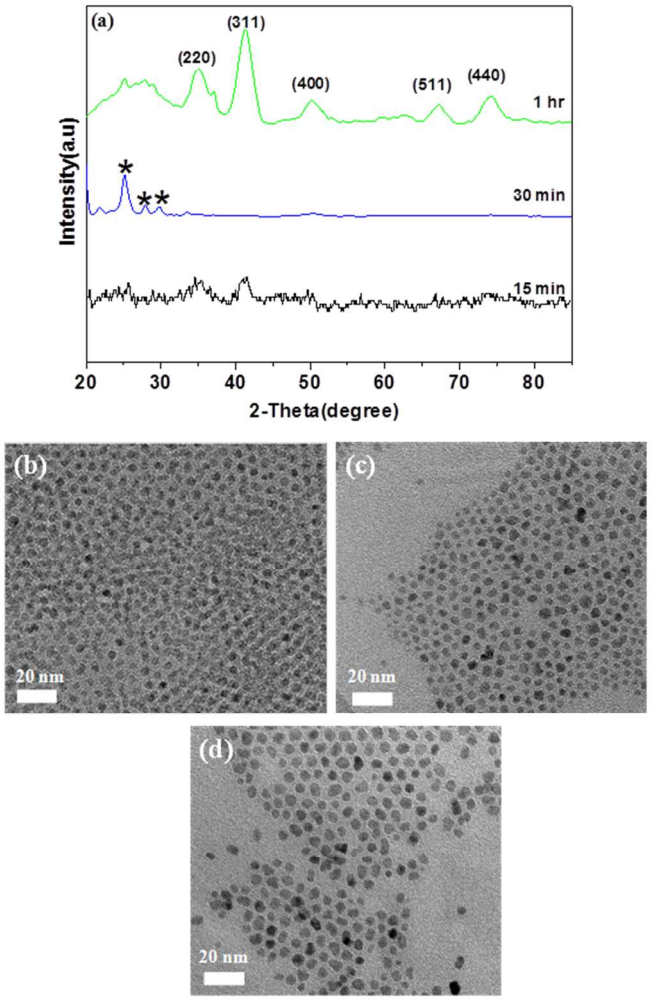

Fig. 1 (a) The p-XRD pattern for cubic iron zinc oxide (Fe_2ZnO_4) nanoparticles from $[Zn_4Fe_2O_2(O_2C^tBu)_{10}]$ at different times prepared by injecting 0.25mmol solution of the precursor at 260 °C.*corresponds to Fe_2O_3 peaks. (b)- (d): TEM images of $ZnFe_2O_4$ withdrawn at 30 minutes, 1 hour and (d) 2 hours respectively.

The p-XRD of the nanoparticles obtained from $[Fe_2NiO(O_2C^tBu)_6(HO_2C^tBu)_3]$ at different times are shown in Fig 2 (a). No product was obtained at 5 minutes. Products obtained at 15 minutes and 30 minutes contain hexagonal iron oxide peaks (ICDD card No: 04-013-3305) whilst the peaks obtained after 1 hour correspond to cubic nickel ferrite (ICDD Card No: 00-054-0964). The intensity, sharpness and crystallinity of the peaks obtained increase over time. The TEM images taken for samples (Fig. 2 (b)-(d)) revealed that average diameter increases over time, images obtained at 30 minutes show nanoparticles with an average diameter of 3.1 ± 0.7 nm, 3.6 ± 0.6 nm at 1 hour and 4.4 ± 0.6 nm at 2 hours.

For both precursors, it was observed that the diameter of the nanoparticles obtained tend to increase over time (Fig. 3). This observation reflects nanoparticle growth.

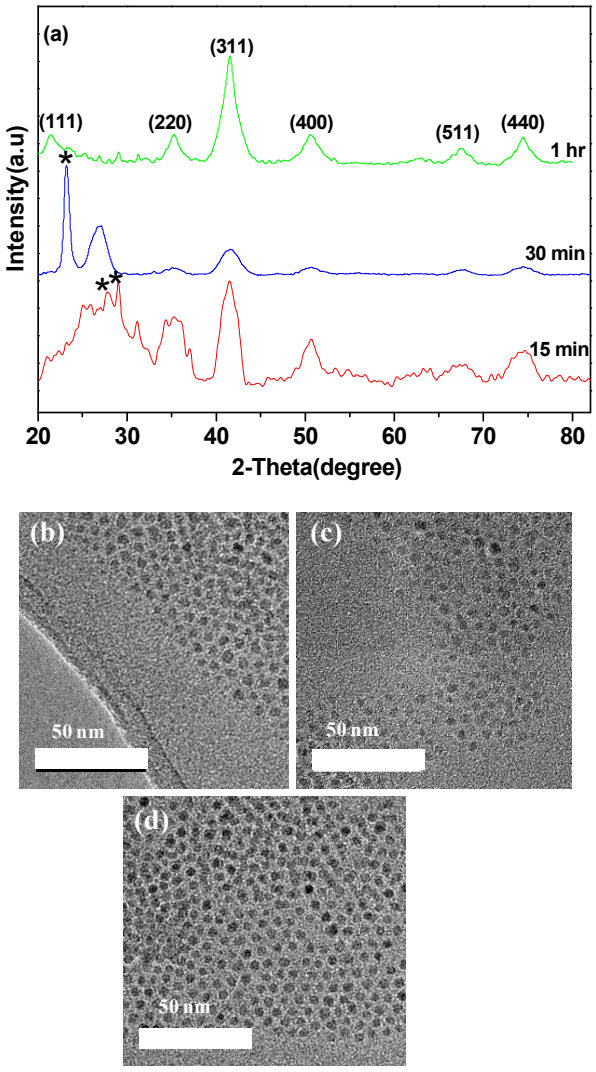

Fig. 2 (a) The p-XRD obtained for cubic nickel ferrite nanoparticles from $[Fe_2NiO(O_2C^tBu)_6(HO_2C^tBu)_3]$ withdrawn at different times. The nanoparticles were prepared by injecting 0.25mmol solution of the precursor at 260 °C. *corresponds to Fe_2O_3 peaks. (b)-(d):TEM images of $NiFe_2O_4$ withdrawn at 30 minutes, 1 hour and 2 hours respectively.

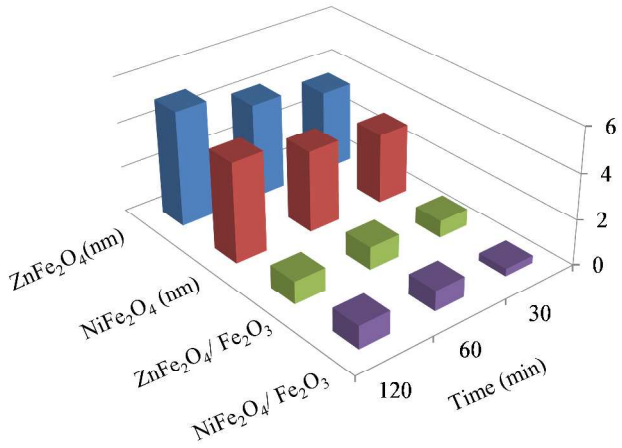

Fig. 3 Graphical representation of different phases and sizes of zinc and nickel ferrite nanoparticles obtained at various reaction times.

Effect of temperature

The effect of temperature was studied for both precursors at the boiling point of two different solvents- diphenyl ether at 260 ºC and benzyl ether at 300 °C at a fixed concentration of 0.25 mmol over 2 hours.

The p-XRD pattern for nanoparticles obtained from $[Zn_4Fe_2O_2(O_2C^tBu)_{10}]$ at both temperatures (260 and 300ºC) were of cubic $Zn_{0.93}Fe_2O_4$ (ICDD card No: 04-006-1956) (Fig. 4(a)). The average crystallite size calculated by the Scherrer equation are: 4 nm for particles obtained at 260 ºC and 5 nm for those obtained at 300 ºC whilst the average diameter calculated from the TEM images for these particles are 5.1 ± 0.7 and 5.6 ± 0.5 nm at 260 °C and 300 °C respectively (Figs. 5(a) and (b)).

The thermolysis of $[Fe_2NiO(O_2C^tBu)_6(HO_2C^tBu)_3]$ at both 260 and 300ºC resulted in nanoparticles with p-XRD pattern corresponding to cubic nickel ferrite (ICDD Card No: 00-054-0964) (Fig. 4(b)). Using Scherrer formula, the particle size was estimated to be 3.8 nm for particles obtained at 260 °C and 5 nm for those obtained at 300 °C. The TEM images showed an increase in diameter with the increase in temperature, nanoparticles obtained at 260 °C have an average diameter of 4.4 ± 0.6 nm whilst 5 ± 0.6 nm was obtained at 300 °C.

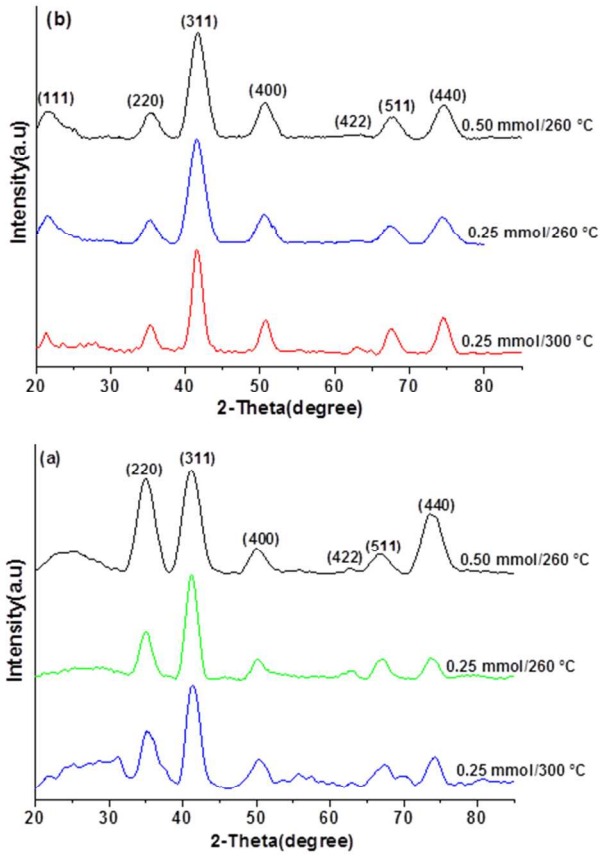

Fig. 4 (a) and (b)**:** the p-XRD pattern for cubic $ZnFe_2O_4$ and Fe_2NiO_4 nanoparticles obtained by the thermolysis of $[Zn_4Fe_2O_2(O_2C^tBu)_{10}]$ and $[Fe_2NiO(O_2C^tBu)_6(HO_2C^tBu)_3]$ respectively in different boiling point solvents of diphenylether (260 °C) or benzyl ether (300 °C).

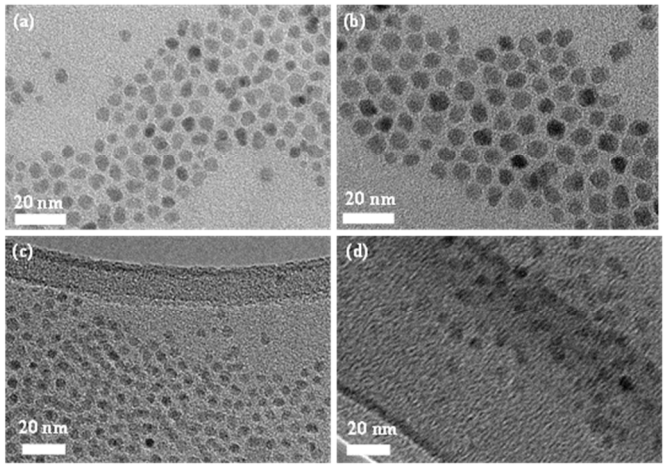

Fig. 5 (a) and (b): TEM images obtained for $Zn_{0.93}Fe_2O_4$ nanoparticles from $[Zn_4Fe_2O_2(O_2C^tBu)_{10}]$ (0.25 mmol) thermolysed in diphenyl ether at 260 °C or benzyl ether at 300 °C respectively.(c) and (d): TEM images obtained for Fe_2NiO_4 nanoparticles from $[Fe_2NiO(O_2C^tBu)_6(HO_2C^tBu)_3]$ (0.25 mmol) thermolysed in diphenyl ether at 260 °C or benzyl ether at 300 °C respectively.

The average diameter calculations from the TEM results obtained in the two cases are in good agreement with those obtained using the Scherrer's equation. The increase in the nanoparticle's diameter with rise in temperature observed for these particles has been reported by us and other researchers.[46–51]

Concentration effects

The effect of concentration on the form and morphology of the ferrite particles was studied for the two precursors by thermolysing 0.25 mmol or 0.50 mmol at 260 ºC for over 2 hours.

Particles from $[Zn_4Fe_2O_2(O_2C^tBu)_{10}]$ (1) at different precursor concentrations

The p-XRD pattern for particles produced from $[Zn_4Fe_2O_2(O_2C^tBu)_{10}]$ at 0.25 mmol corresponds to cubic $Zn_{0.93}Fe_2O_4$ (ICDD card No: 04-006-1956) whilst those obtained at 0.50 mmol were of Franklinite, $ZnFe_2O_4$ (ICDD card No: 01-070-6393) (Fig. 4(a)). The average diameters calculated by the Scherrer's equation are: 3 and 4 nm for nanoparticles obtained from 0.50 and 0.25 mmol respectively.

TEM images revealed that Zn1 ($ZnFe_2O_4$ nanoparticles obtained with 0.50 mmol) have improved monodispersity with an average diameter of 3.2 ± 0.2 nm whilst Zn2 ($Zn_{0.93}Fe_2O_4$ produced at 0.25 mmol) have an average diameter of 5.1 ± 0.7 nm. The TEM analysis is in good agreement with the calculated sizes from the Scherrer equation. The synthesised nanoparticles are crystalline as seen in the lattice fringes with a *d*-spacing of 2.98 Å which is very close to the (220) reflection of zinc iron oxide (ICDD Card No: 01-070-6393) (Fig. 6(a)). Zn1 and Zn2 correspond to zinc ferrite nanoparticles obtained from 0.50 mmol and 0.25 mmol precursor concentrations respectively. Our nanoparticles show a very good size distribution and are spherical compared to those previously reported using solvothermal method.[15,27]

Magnetic properties of zinc ferrite nanoparticles from $[Zn_4Fe_2O_2(O_2C^tBu)_{10}]$ (1)

Magnetic measurements of $ZnFe_2O_4$ obtained from $[Zn_4Fe_2O_2(O_2C^tBu)_{10}]$ are superparamagnetic at room temperature, that is, the orientation of their magnetic moments responds freely to thermal fluctuations. An estimate for the blocking temperature (T_B) of the samples was done and the data showed that T_B increases with increasing nanoparticle diameter, ranging from 10 K for $ZnFe_2O_4$ with an average diameter of 3.2 nm to 20 K for $ZnFe_2O_4$ with an average diameter of 5.1 nm (Fig. 6(c)). Above the blocking temperature, the thermal energy is enough to overcome the anisotropy energy barrier of the particles, thus the remanent magnetisation tend towards zero and the particles are said to exhibit superparamagnetism.[52]

Field dependent magnetisation studies performed at temperatures of 5 and 300 K on zinc ferrite nanoparticles showed that the saturation magnetisation (M_s) increases with the average particle diameter at both temperatures (Fig. 6(b)). $ZnFe_2O_4$ of average diameter 3.2 nm are characterised by M_s values of 59 (5 K) and 22 emu/g (300 K) whilst those of $ZnFe_2O_4$ with average diameter of 5.3 nm exhibit M_S values of 87 (5 K) and 37 emu/g (300 K).

The magnetisation *versus* field measurements at 5 K for zinc ferrite nanoparticles display a hysteresis loop with a coercive field (H_c) (*i.e.* the magnetic field needed for the magnetisation to return to zero) and remanent magnetisation (M_R) (*i.e.* the magnetisation retained by nanoparticles when the magnetic field is switched off) of *ca.* 0.14 kOe and 11.5 emu/g respectively for nanoparticles of average diameter 5.1 nm whilst the remanence and coercivity of zinc ferrite nanoparticles of average diameter 3 nm are negligible.

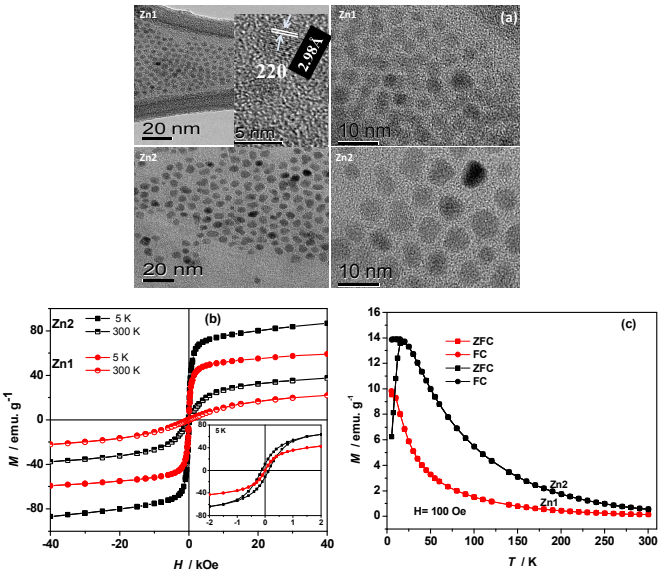

Fig. 6 (a) TEM and HRTEM images of $ZnFe_2O_4$ at 260 °C over 2 hours. Zn1 and Zn2 correspond to zinc ferrite nanoparticles obtained from 0.50 mmol and 0.25 mmol precursor concentrations respectively, (b) the hysteresis loops measured at 5 and 300 K for Zn1 of average diameter 3.2 ± 0.2 nm and Zn2 of average diameter 5.1 ± 0.7 nm (c) Zero field cooled (ZFC) and Field-cooled (FC) magnetisation curves for Zn1 and Zn2.

Bulk zinc ferrite has a normal spinel structure with the absence of Fe^{3+} ions in the tetrahedral sites thus making zinc ferrite antiferromagnetic below 10 K. However, in our zinc ferrite nanoparticles, the saturation magnetisation values and coercivity are enhanced. This can be explained by the cation redistribution, involving migration of some Fe^{3+} ions to the tetrahedral sites thereby creating a stronger ferrimagnetic interaction between the Fe^{3+} ions in tetrahedral and octahedral sites.[32,53,54]

Particles from $[Fe_2NiO(O_2C^tBu)_6(HO_2C^tBu)_3]$ (2) at different concentrations

The p-XRD pattern for particles obtained from $[Fe_2NiO(O_2C^tBu)_6(HO_2C^tBu)_3]$ at both 0.50 and 0.25 mmol were matched with cubic $NiFe_2O_4$ (ICDD card No: 00-054-0964) (Fig. 4(b)). The average diameters of the nanoparticles calculated by the Scherrer equation are: 3.3 and 3.8 nm respectively for nanoparticles obtained from 0.50 and 0.25 mmol precursor concentrations. TEM images showed monodispersed nanoparticles were obtained from both precursor concentrations but with smaller sizes at higher concentration. The average diameter estimated from the TEM are 3.3 ± 0.2 nm (Ni1) and 4.4 ± 0.5 nm (Ni2) at 0.50 and 0.25 mmol respectively (Fig. 7(a)). The lattice fringes of the nanoparticles are distinct, indicating the high crystallinity of the nickel ferrite nanoparticles. A d-spacing value of 2.512 Å was obtained which is the same as the (311) reflection of nickel iron oxide (ICDD Card No: 00-054-0964) (Fig. 7(a)). Our results showed that nickel ferrite nanoparticles prepared by the hot injection thermal decomposition have superior

monodispersity and without aggregation compared with those prepared using the sol-gel method.[22]

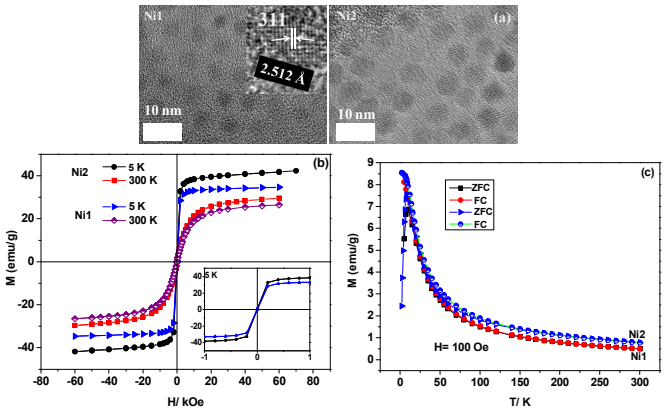

Fig. 7 (a) TEM and HRTEM images of $NiFe_2O_4$ obtained at 260 °C over 2 hours. Ni1 and Ni2 are the nickel ferrite nanoparticles obtained from 0.50 mmol and 0.25 mmol precursor concentrations respectively, (b) the hysteresis loops measured at 5 and 300 K for Ni1 of average diameter 3.2 ± 0.2 nm and Ni2 of average diameter 5.1 ± 0.7 nm (c) Zero field cooled (ZFC) and Field-cooled (FC) magnetisation curves for Ni1 and Ni2.

Magnetic properties of nickel ferrite nanoparticles from (2)

Magnetic measurements were performed on $NiFe_2O_4$ nanoparticles; Ni1 (from 0.50 mmol) with average diameters 3.3 ± 0.2 nm and Ni2 (from 0.25 mmol) of average diameter 4.4 ± 0.5 nm. The blocking temperature of both Ni1 and Ni2 nanoparticles is about 11 K, both are well defined indicating a narrow distribution of particle diameters (Fig. 7(c)). Above the blocking temperature, the magnetisation orientations average to zero and the nanoparticles become superparamagnetic. The saturation magnetisation values were measured for these nanoparticles at 5 K and 300 K. For Ni1 (average diameter 3.3 nm) 34 and 26.5 emu/g were recorded, whilst for Ni2, (average diameter 4.4 nm) 42 and 29.3 emu/g values were obtained (Fig. 7(b)). The coercivity and remanence of these nanoparticles are negligible at both temperatures.

Bulk nickel ferrite has a saturation magnetisation value of about 56 emu/g[54] which is higher than the values obtained for our nanoparticles. This difference is usually observed in nanoparticles and is most likely attributed to the existence of organic coating agents and intrinsic canted spins on the surface of such small nanoparticles.[55]

ICP-OES, EPMA and XMCD analysis of zinc ferrite and nickel ferrite nanoparticles

ICP-OES analysis showed that the [Fe]: [Zn] is approximately 2: 1 for Zn1 ($ZnFe_2O_4$ nanoparticles obtained at 0.50 mmol). In addition, the [Fe]: [Zn] of the nanoparticles were determined using EPMA, and this were found to be 2.2: 0.7 for Zn1, slightly lower in Zn than indicated by ICP-OES.

XMCD of iron is dependent upon the magnetic moments of the Fe in the two sub-lattices in the ferrite structure, (spin up and spin down), valence state (via the number of *d* electrons) and site symmetry (crystal field).[56] Thus the distribution of Fe cations within the magnetite structure can be determined by comparison of the XMCD to atomic multiplet calculations.[56,44] The technique has been used successfully to determine site occupancies in ferrite spinels[43,57] and nanoparticulate bio-ferrites.[52,58]

The Fe $L_{2,3}$-edge XAS of the Zn1 sample (Fig. 8(a)) has a small shoulder on the low energy side of the L_3-edge which is similar to that seen in the XAS of Fe^{3+} oxide minerals such as goethite and ferrihydrite and held as indicative of the presence of more Fe^{3+} than in stoichiometric magnetite. This excess could be the result of either surface oxidation by air exposure or the presence of a cation (such as Zn^{2+}) replacing the Fe^{2+} within the spinel structure, altering the ratio of Fe^{2+}: Fe^{3+}, and giving a spectral shape dominated by oxidised iron. Examination of the XMCD spectra (Fig. 8(b)) show three peaks derived from the Fe L_3-edge characteristic of the three iron structural environments within magnetite. These can be fitted using multiplet calculations for the three iron environments to give the quantitative data shown in Table 1. These data indicate that the magnetite is deficient in both $Fe^{2+}O_h$ and $Fe^{3+}T_d$, but has excess $Fe^{3+}O_h$. This suggests that there is partial oxidation of Fe^{2+} to Fe^{3+} within the structure but the amount of excess Fe^{3+} in O_h sites cannot account for all the 'missing' Fe^{2+} in O_h geometry. It can therefore be assumed that at least some of the sites that would normally be occupied by Fe^{2+} contain Zn as is supported by the magnetometry measurements. In addition, since Zn has a strong affinity for T_d sites[59] it is unsurprising that there is a deficit of Fe^{3+} due to Zn substitution. It should be noted that Fe ratios suggest 0.34 cations of Zn are in the T_d site and using the EPMA data, half of the Zn resides in O_h geometry.

ICP-OES analysis showed that the ratio of Fe to Ni is approximately 2: 1 for $NiFe_2O_4$ particles obtained at a higher precursor concentration (Ni1). The Ni $L_{2,3}$-edge XAS spectra (Fig. 8(c)) are indicative of Ni^{2+} in an octahedral environment as it is similar to the spectral shape in Coker *et al.*[58] which agrees with calculations for this Ni environment in van der Laan and Kirkman.[44] Both samples are similar and the presence of XMCD at the Ni $L_{2,3}$-edge, the Ni is therefore magnetic and that Ni has been incorporated into the spinel structure in the expected coordination and geometry.

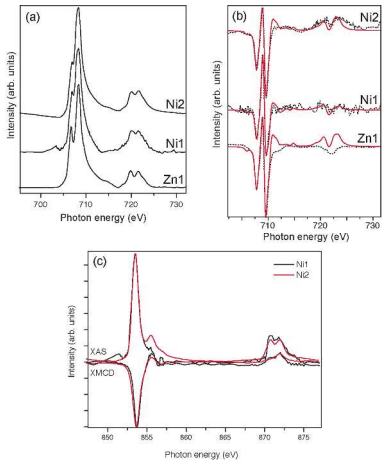

Fig. 8 Fe $L_{2,3}$-edge (a) isotropic XAS and corresponding (b) XMCD for samples Zn1, Ni1 and Ni2, data (black) and XMCD calculated fits (red). (c) Ni $L_{2,3}$-edge XAS and XMCD for Ni1 (black) and Ni2 (red)

This result is confirmed by quantitative fitting of the respective Fe $L_{2,3}$-edge XMCD spectra for each of the samples (Fig. 8(b); Table

1, which show a deficit in Fe^{2+} in O_h geometry within the spinel, suggesting substitution by the Ni cation. The Fe L_3-edge XAS (Fig. 8(a)) has a shoulder feature on the low energy side as seen above in the Zn samples, with Ni2 having a more pronounced feature. Again this shows that the sample is oxidised compared to stoichiometric magnetite, which would be expected if Ni^{2+} is substituting for Fe^{2+} in the spinel structure.

Table 1. Fe site occupancies determined using Fe^{+}cation ratios, XMCD spectra and atomic multiplet calculations.

Precursor (Sample)	Conc(mmol)	Fe+Co = 3 (EPMA)		Ratios	Fe site occupancies			
		Fe	Zn	Fe^{2+}/Fe^{3+}	T_d/O_h	Fe^{2+} O_h	Fe^{3+} T_d	Fe^{3+} O_h
$[Zn_4Fe_2O_2(O_2C^tBu)_{10}]$ **(Zn1)**	0.50	2.2	0.7	0.21	0.43	0.38	0.66	1.17
$[Zn_4Fe_2O_2(O_2C^tBu)_{10}]$ **(Zn2)**	0.25							
		Fe	**Ni**					
$[Fe_2NiO(O_2C^tBu)_6(HO_2C^tBu)_3]$ **(Ni1)**	0.50	2.12	0.88	0.18	0.72	0.37	1.03	1.07
$[Fe_2NiO(O_2C^tBu)_6(HO_2C^tBu)_3]$ **(Ni2)**	0.25			0.22	0.44	0.41	0.69	1.17
Magnetite		3	0	0.5	0.5	1	1	1

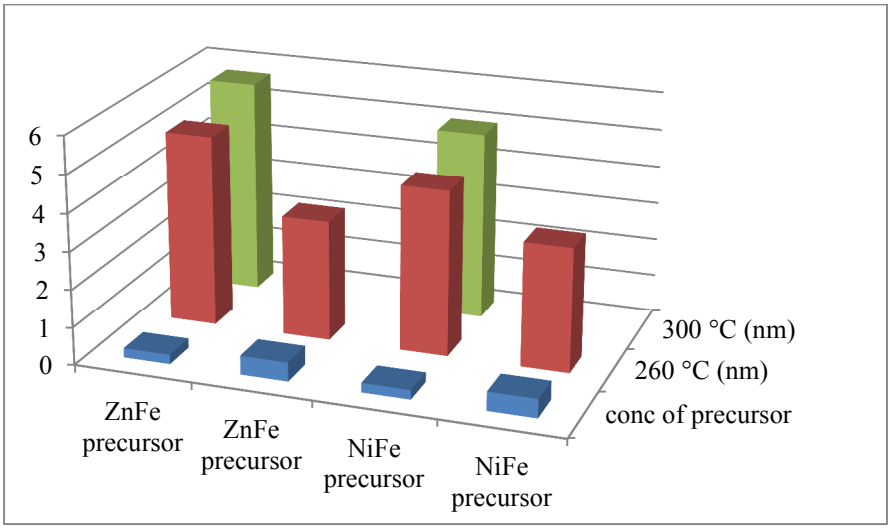

Fig. 9 Graphical representation of different sizes of zinc and nickel ferrite nanoparticles obtained by varying precursor concentration and temperature.

Conclusions

The bimetallic pivalate clusters of $[Zn_4Fe_2O_2(O_2C^tBu)_{10}]$ **(1)** and$[Fe_2NiO(O_2C^tBu)_6(HO_2C^tBu)_3]$ **(2)** were used as single source precursors for the direct synthesis of zinc and nickel ferrite nanoparticles. Highly monodispersed zinc ferrite and nickel ferrite nanoparticles were obtained from precursors **(1)** or **(2)** at 0.50 mmol. The effect of decomposition temperature studied for the three precursors revealed that larger nanoparticles of zinc and manganese ferrites were obtained at 300 °C at 0.25 mmol from **(1)** or **(2)**. A mixture of iron oxide and the corresponding ternary oxide were obtained at reaction times of less than 1 hour in both cases whilst the pure ferrite was obtained after 1 hour.

XMCD analysis established that the majority of Ni^{2+} is in octahedral sites in the nickel ferrite nanoparticles. The hysteresis loop observed in the zinc ferrite nanoparticles indicates that there is a cation redistribution i.e. some of the Zn cations are in the

octahedral sites: this is further evident in the EPMA result and XMCD analysis.

Acknowledgement

K.O. A. gratefully acknowledges the financial support from the Islamic Development Bank, Saudi Arabia.

The XAS and XMCD were carried out at the Advanced Light Source supported by the Director, Office of Science, Office of Basic Energy Sciences, of the U.S. Department of Energy under contract No. DE-AC02-05CH11231.

Notes and References

[a] School of Chemistry, University of Manchester, Oxford Road, Manchester, M13 9PL, UK.
[b] School of Materials, University of Manchester, Grosvenor Street, Manchester, M1 7HS, UK.
[c] The Photon Science Institute, University of Manchester, Oxford Road, Manchester, M13 9PL, UK.
[d] School of Earth, Atmospheric and Environmental Sciences and Williamson Research Centre for Molecular Environmental Science, University of Manchester, Manchester, M13 9PL, UK
[e] Advanced Light Source, Lawrence Berkeley National Lab., Berkeley, CA 94720, USA
EMAIL: paul.obrien@manchester.ac.uk

References

1. Y. Kinemuchi, K. Ishizaka, H. Suematsu, W. Jiang, and K. Yatsui, *Thin Solid Films*, 2002, **407**, 109.
2. S. P. Gubin, Y. I. Spichkin, G. Y. Yurkov, and A. M. Tishin, *Russ. J. Inorg. Chem.*, 2002, **47**, 32.
3. X. Li, G. Tan, W. Chen, B. Zhou, D. Xue, Y. Peng, F. Li, and N. J. Mellors, *J. Nanoparticle Res.*, 2012, **14**, 751.
4. D. S. Mathew and R.-S. Juang, *Chem. Eng. J.*, 2007, **129**, 51.
5. J. Hong, D. Xu, J. Yu, P. Gong, H. Ma, and S. Yao, *Nanotechnology*, 2007, **18**, 135608.
6. J.-H. Park, G. von Maltzahn, L. Zhang, M. P. Schwartz, E. Ruoslahti, S. N. Bhatia, and M. J. Sailor, *Adv. Mater.*, 2008, **20**, 1630.
7. R. F. Ziolo, E. P. Giannelis, B. A. Weinstein, M. P. O'Horo, B. N. Ganguly, V. Mehrotra, M. W. Russell, and D. R. Huffman, *Science* , 1992, **257**, 219.
8. X. Shi, S. H. Wang, S. D. Swanson, S. Ge, Z. Cao, M. E. Van Antwerp, K. J. Landmark, and J. R. Baker, *Adv. Mater.*, 2008, **20**, 1671.
9. M. M. Rashad and O. A. Fouad, *Mater. Chem. Phys.*, 2005, **94**, 365.
10. L. Satyanarayana, K. M. Reddy, and S. V. Manorama, *Mater. Chem. Phys.*, 2003, **82**, 21.
11. P. Lavela and J. L. Tirado, *J. Phys. Chem. C*, 2010, **114**, 12828.
12. P. Sivakumar, R. Ramesh, A. Ramanand, S. Ponnusamy, and C. Muthamizhchelvan, *J. Mater. Sci. Mater. Electron.*, 2011, **23**, 1041.
13. K. Maaz, S. Karim, A. Mumtaz, S. K. Hasanain, J. Liu, and J. L. Duan, *J. Magn. Magn. Mater.*, 2009, **321**, 1838.
14. W. Cheng, K. Tang, and J. Sheng, *Chem. Eur. J.*, 2010, **16**, 3608.
15. L. Chen, Y. Shen, and J. Bai, *Mater. Lett.*, 2009, **63**, 1099.
16. J. Wang, *Mater. Sci. Eng. B*, 2006, **127**, 81.
17. K. Nejati and R. Zabihi, *Chem. Cent. J.*, 2012, **6**, 23.
18. Y. Cheng, Y. Zheng, Y. Wang, F. Bao, and Y. Qin, *J. Solid State Chem.*, 2005, **178**, 2394.
19. J. Huo and M. Wei, *Mater. Lett.*, 2009, **63**, 1183.
20. A. Baykal, N. Kasapoğlu, Y. Köseoğlu, M. S. Toprak, and H. Bayrakdar, *J. Alloys Compd.*, 2008, **464**, 514.
21. S. Yáñez-Vilar, M. Sánchez-Andújar, C. Gómez-Aguirre, J. Mira, M. A. Señarís-Rodríguez, and S. Castro-García, *J. Solid State Chem.*, 2009, **182**, 2685.
22. P. Sivakumar, R. Ramesh, A. Ramanand, S. Ponnusamy, and C. Muthamizhchelvan, *Mater. Res. Bull.*, 2011, **46**, 2204.
23. M. Srivastava, A. K. Ojha, S. Chaubey, and A. Materny, *J. Alloys Compd.*, 2009, **481**, 515.
24. T. Sato, K. Sue, W. Suzuki, M. Suzuki, K. Matsui, Y. Hakuta, H. Hayashi, K. Arai, S. Kawasaki, A. Kawai-Nakamura, and T. Hiaki, *Ind. Eng. Chem. Res.*, 2008, **47**, 1855.
25. R. A. D. Pattrick, V. S. Coker, C. I. Pearce, N. D. Telling, G. van der Laan, and J. R. Lloyd, *Nanoscience*, 2012, **1**, 114.
26. S. Mohapatra, S. R. Rout, and A. B. Panda, *Colloids Surfaces A Physicochem. Eng. Asp.*, 2011, **384**, 453.
27. K. P. Naidek, F. Bianconi, T. C. R. da Rocha, D. Zanchet, J. A. Bonacin, M. A. Novak, M. D. G. F. Vaz, and H. Winnischofer, *J. Colloid Interface Sci.*, 2011, **358**, 39.
28. N. Bao, L. Shen, Y. Wang, P. Padhan, and A. Gupta, *J. Am. Chem. Soc.*, 2007, **129**, 12374.
29. M. Moriya, M. Ito, W. Sakamoto, and T. Yogo, *Cryst. Growth Des.*, 2009, **9**, 1889.
30. H. Ehrhardt, S. J. Campbell, and M. Hofmann, *Scr. Mater.*, 2003, **48**, 1141.
31. S. Bid and S. K. Pradhan, *Mater. Chem. Phys.*, 2003, **82**, 27.
32. Y. Xu, Y. Liang, L. Jiang, H. Wu, H. Zhao, and D. Xue, *J. Nanomater.*, 2011, **2011**, 1.
33. C. Bárcena, A. K. Sra, G. S. Chaubey, C. Khemtong, J. P. Liu, and J. Gao, *Chem. Commun.*, 2008, 2224.
34. R. Zhang, J. Huang, J. Zhao, Z. Sun, and Y. Wang, *Energy and Fuels*, 2007, **21**, 2682.
35. F. Gao, X. Y. Chen, K. B. Yin, S. Dong, Z. F. Ren, F. Yuan, T. Yu, Z. G. Zou, and J. M. Liu, *Adv. Mater.*, 2007, **19**, 2889.
36. M. Milanović, E. G. Moshopoulou, D. Stamopoulos, E. Devlin, K. P. Giannakopoulos, A. G. Kontos, K. Eleftheriadis, M. I. Gini, and L. M. Nikolić, *Ceram. Int.*, 2013, **39**, 3235.
37. C. A. Ladole, *Int. J. Chem. Sci.*, 2012, **10**, 1230.
38. M. Veith, M. Haas, and V. Huch, *Chem. Mater.*, 2005, **17**, 95.
39. J. W. Moon, Y. Roh, R. J. Lauf, H. Vali, L. W. Yeary, and T. J. Phelps, *J. Microbiol. Methods*, 2007, **70**, 150.
40. L. W. Yeary, J. W. Moon, C. J. Rawn, L. J. Love, A. J. Rondinone, J. R. Thompson, B. C. Chakoumakos, and T. J. Phelps, *J. Magn. Magn. Mater.*, 2011, **323**, 3043.
41. F. Grasset, N. Labhsetwar, D. Li, D. C. Park, N. Saito, H. Haneda, O. Cador, T. Roisnel, S. Mornet, E. Duguet, J. Portier, and J. Etourneau, *Langmuir*, 2002, **18**, 8209.
42. J. Wan, X. Jiang, H. Li, and K. Chen, *J. Mater. Chem.*, 2012, **22**, 13500.

43. R. A. D. Pattrick, G. Van Der Laan, C. M. B. Henderson, P. Kuiper, E. Dudzik, and D. J. Vaughan, *Eur. J. Mineral.*, 2002, **14**, 1095.
44. G. van der Laan and I. W. Kirkman, *J. Phys. Condens. Matter*, 1992, **4**, 4189.
45. E. Rentschler, A. S. Batsanov, G. A. Timco, T. Weyermuller, and R. E. P. Winpenny, in *Book of abstracts of the XIV- th Conference on Physical Methods in Coordination and Supramolecular Chemistry*, Chisinau, Moldova, 2002, pp. 82, 166.
46. K. O. Abdulwahab, M. A. Malik, P. O'Brien, G. A. Timco, F. Tuna, C. A. Muryn, R. E. P. Winpenny, R. A. D. Pattrick, V. S. Coker, and E. Arenholz, *Chem. Mater.*, 2014, **26**, 999.
47. K. Abdulwahab, M. A. Malik, P. O'Brien, K. Govender, C. A. Muryn, G. A. Timco, F. Tuna, and R. E. P. Winpenny, *Dalt. Trans.*, 2013, **42**, 196.
48. C. Burda, X. Chen, R. Narayanan, and M. A. El-Sayed, *Chem. Rev.*, 2005, **105**, 1025.
49. N. Bao, L. Shen, W. An, P. Padhan, C. Heath Turner, and A. Gupta, *Chem. Mater.*, 2009, **21**, 3458.
50. J. Park, K. An, Y. Hwang, J.-G. Park, H.-J. Noh, J.-Y. Kim, J.-H. Park, N.-M. Hwang, and T. Hyeon, *Nat. Mater.*, 2004, **3**, 891.
51. W. W. Yu, J. C. Falkner, C. T. Yavuz, and V. L. Colvin, *Chem. Commun.*, 2004, 2306.
52. V. S. Coker, N. D. Telling, G. van der Laan, R. A. D. Pattrick, C. I. Pearce, E. Arenholz, F. Tuna, R. E. P. Winpenny, and J. R. Lloyd, *ACS Nano*, 2009, **3**, 1922.
53. R. Sai, S. D. Kulkarni, K. J. Vinoy, N. Bhat, and S. A. Shivashankar, *J. Mater. Chem.*, 2012, **22**, 2149.
54. A. Kundu, C. Upadhyay, and H. C. Verma, *Phys. Lett. A*, 2003, **311**, 410.
55. K. Maaz, A. Mumtaz, S. K. Hasanain, and A. Ceylan, *J. Magn. Magn. Mater.*, 2007, **308**, 289.
56. G. van derLaan and B. T. Thole, *Phys. Rev. B*, 1991, **43**, 13401.
57. C. I. Pearce, C. M. B. Henderson, R. A. D. Pattrick, G. Van der Laan, and D. J. Vaughan, *Am. Mineral.*, 2006, **91**, 880.
58. V. S. Coker, C. I. Pearce, R. A. D. Pattrick, G. van der Laan, N. D. Telling, J. M. Charnock, E. Arenholz, and J. R. Lloyd, *Am. Mineral.*, 2008, **93**, 1119.
59. V. G. Harris, N. C. Koon, C. M. Williams, Q. Zhang, M. Abe, and J. P. Kirkland, *Appl. Phys. Lett.*, 1996, **68**, 2082.